SUPPLEMENT TO THE *WELDING JOURNAL,* APRIL 2008
Sponsored by the American Welding Society and the Welding Research Council

Measurement and Analysis of Three-Dimensional Specular Gas Tungsten Arc Weld Pool Surface

Two reconstruction schemes were verified as valid means of rebuilding a three-dimensional weld pool surface off-line

BY H. S. SONG AND Y. M. ZHANG

ABSTRACT. Measurement of weld pool surface is a difficult but urgent task in the welding community. It plays an important role not only in developing the next-generation intelligent welding machines but also for modeling complex welding processes. In recent years, different techniques have been applied in this area, but the specular characteristic of weld pool surface and the strong welding arc compromise their effectiveness. To better resolve this problem, a new vision-based sensing (measurement) system was proposed in our previous study, which utilizes the reflection property of the weld pool surface. In that system, a dot-matrix pattern of structured laser light was projected onto the specular weld pool surface and its reflection was imaged on a self-designed imaging plane. Then the distorted reflected image (pattern) was captured and processed. Based on the obtained information, two reconstruction schemes named interpolation reconstruction scheme (IRS) and extrapolation reconstruction scheme (ERS), are proposed in this paper in order to rebuild the three-dimensional weld pool surface off-line. The experimental results verify the effectiveness of the proposed methods and show that ERS can achieve better accuracy than IRS. Meanwhile, the variation of the weld pool surface in an experiment is also analyzed by using the proposed measurement system and extrapolation reconstruction scheme.

*H. S. SONG and Y. M. ZHANG (*ymzhang@engr.uky.edu*) are with Center for Manufacturing and Department of Electrical and Computer Engineering, University of Kentucky, Lexington, Ky.*

Introduction

Welding is a labor-intensive operation. Although welding robots can provide consistent motion to help improve productivity, they lack the intelligence that human welders possess to ensure quality. Since skilled human welders can achieve good weld quality through observing the weld pool, the pool surface must contain sufficient information to judge weld quality, such as weld joint penetration. Meanwhile, the precise measurement of the weld pool surface can provide critical experimental data to validate numerical models of welding processes. Hence, the measurement of three-dimensional weld pool surface is a fundamental capability that the next-generation automated welding machines and welding researchers must possess, and a number of early efforts have been devoted to sensing weld pool related parameters including machine vision, X-ray radiation, ultrasonic, and acoustic emission (Refs. 1–4).

Among these methods, noncontact vision-based ones have been studied more extensively (Refs. 5–11). An important technique for a 2-D weld pool boundary measurement is the coaxial viewing of the weld pool, which was first proposed by Richardson et al. (Ref. 5). It has been widely investigated by some researchers. In the coaxial viewing method, the electrode is used to block the arc, but the image quality is decreased by the bright plasma. Agapakis and Bolstad presented an innovative vision sensing system that used intense stroboscopic illumination to overpower the arc light in the welding process and produce a clear image with synchronized camera (Ref. 6). This technique was further applied in the Welding Research Laboratory at the University of Kentucky by Kovacevic and Zhang.

The acquired image is shown in Fig. 1A and an image processing algorithm has been developed to analyze and extract the two-dimensional boundary of the weld pool so that control algorithms can use these parameters as feedback to adjust welding parameters (Ref. 7). To use this system in three-dimensional weld pool surface imaging, the structured illumination laser was projected through a frosted glass (Ref. 8), and an image with the three-dimensional shape information of weld pool surface was acquired as shown in Fig. 1B. Because of its cost and size, this specially designed system is not suitable for production.

In a separate effort, Mnich and his colleagues (Ref. 9) used stereovision to determine the three-dimensional shape of the weld pool in the GMAW process, but the complexity compromised its suitability for practical application. Another effort by Yoo and Lee (Ref. 10) used a similar principle but introduced the biprism technique to reduce the number of needed cameras from two to one. The accuracy of the system as mentioned by the authors is reasonable.

KEYWORDS

Weld Pool Surface
Specular Reflection
Three-Dimensional
Interpolation
Extrapolation
Surface Variation
GTAW
Control

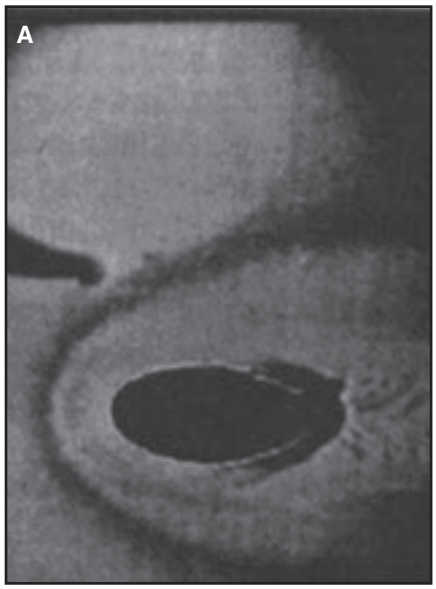

Fig. 1 — Captured images for weld pool measurement. A — 2-D measurement (Ref. 7); B — 3-D measurement (Ref. 8).

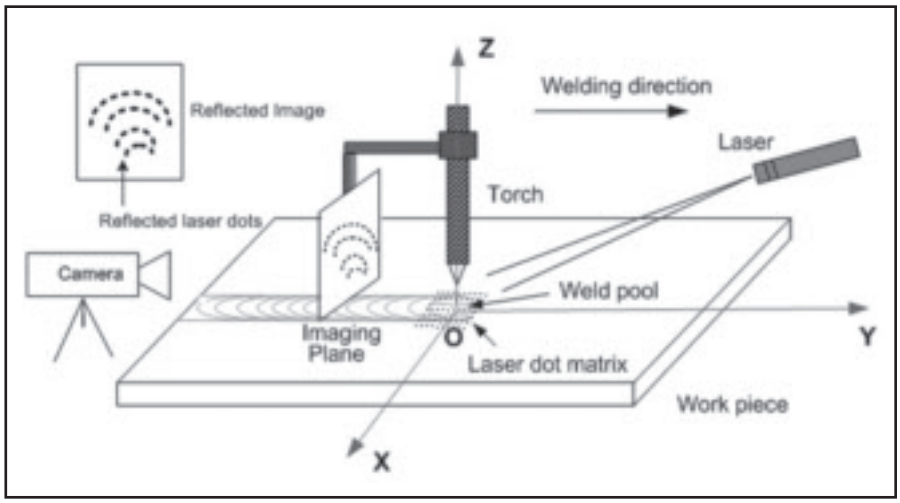

Fig. 2 — Sensing system diagram.

A structured light technique was used by Saeed et al. to determine the profile of the weld pool surface (Ref. 4). In the acquired image, the distortion of the projected laser line clearly showed the shape of the weld pool, while the unavoidable bright arc affected the observation. Another vision-based sensing system was developed for pulsed GTAW with wire filler metal by Zhao et al., which used an improved shape from shading (SFS) algorithm to recover the weld pool surface height (Ref. 11). While all these methods have achieved certain success, more accurate and direct methods are still desired.

The authors recently proposed a different approach to observe the weld pool surface (Refs. 12, 13). It projects a low-power continuous structured laser pattern onto the weld pool surface and intercepts the reflection of the projected pattern from the specular weld pool surface. Because the arc radiation decays very fast with the travel distance while the reflection of the projected laser light remains intense, it is possible that the reflection of the projected laser can be clearly imaged on the interception plane. Since the small low-power laser diode is economical and compact, this approach is more cost-effective, convenient, and suitable for manufacturing applications. However, although the formation of the image is simply based on the reflection law, the reflected image itself does not provide an intuitive view about the dimensions of the weld pool surface. Thus, a reconstruction scheme is needed to derive the three-dimensional shape of the weld pool surface.

In this paper, two schemes named interpolation reconstruction scheme (IRS) and extrapolation reconstruction scheme (ERS) are proposed. Their difference lies in the methods of reconstructing the pool surface and determining the surface boundary. Experimental results verified the accuracy of both methods, and the extrapolation reconstruction scheme proved the better performer.

Sensing System Review

There are three major sequential steps for using the proposed method to reconstruct/measure the pool surface. The first one is to image the laser pattern reflected from the weld pool surface. Then, the acquired reflected image is processed to extract the information of the reflected laser pattern. The third step is to use the three-dimensional reconstruction scheme to rebuild the weld pool surface based on obtained data. The first two major steps are briefly reviewed in this section. Detailed procedures can be found in the literature (Refs. 12–14).

The proposed weld pool surface sensing system in a universal coordinate system is shown in Fig. 2 (Refs. 12, 13). The gas tungsten arc welding (GTAW) process without filler metal was used. The welding direction was along the positive Y axis. A 20-mW continuous illumination laser with a wavelength of 685 nm was used to project a 19 × 19 dot-matrix structured-light pattern onto the weld pool area under the electrode at a certain angle. The interbeam angle of the laser pattern was 0.77 deg. During the welding process, the molten specular weld pool surface can reflect the majority of the incident laser light. Thus, on the other side of the torch, an imaging plane (a piece of glass attached with a grid paper) was placed about 50 mm away in order to intercept the reflected laser pattern. A high-speed camera was used to record the reflected images on the imaging plane. To minimize the influence of the strong arc, the camera was fitted with a 20-nm band-pass filter centered at a wavelength of 685 nm.

In one of the experiments, the laser was projected onto the workpiece at 31.14 deg with a distance of 31.48 mm to the origin of the coordinate system. Figure 3A and B shows the projected pattern and the acquired reflected image. As can be seen, only part of the projected dots located within the weld pool area was reflected, and the laser pattern was shaped by the weld pool surface as convex curves. Although the intensity of the reflected dots was low, the reflected image can still be processed by the proposed algorithms as shown in Fig. 3C.

After image acquisition, a point locat-

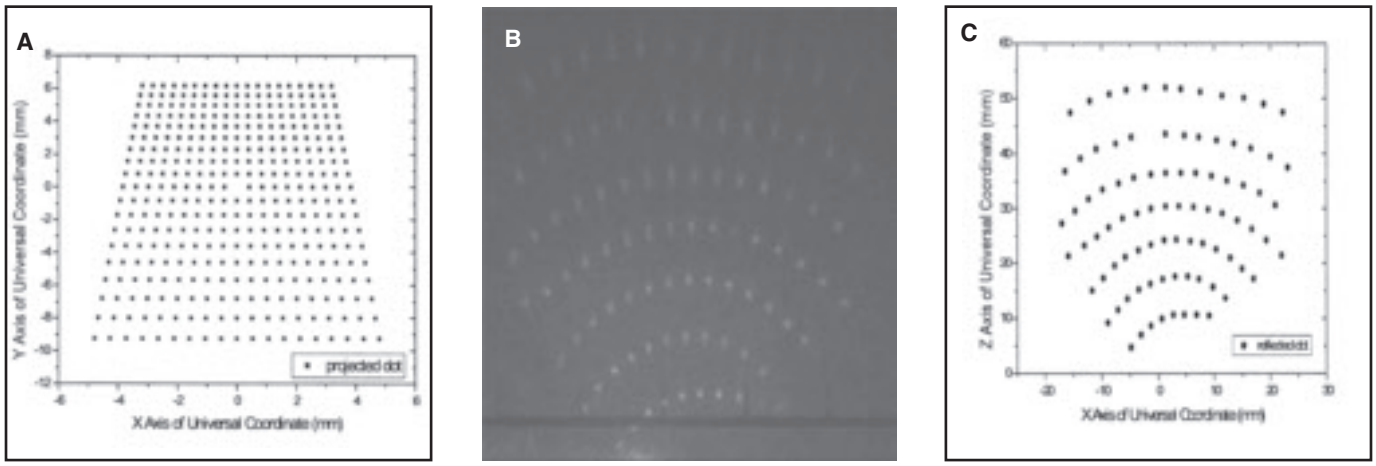

Fig. 3 — Captured and processed images. A — Projected dot-matrix on workpiece; B — captured image; C — reflected dots on imaging plane.

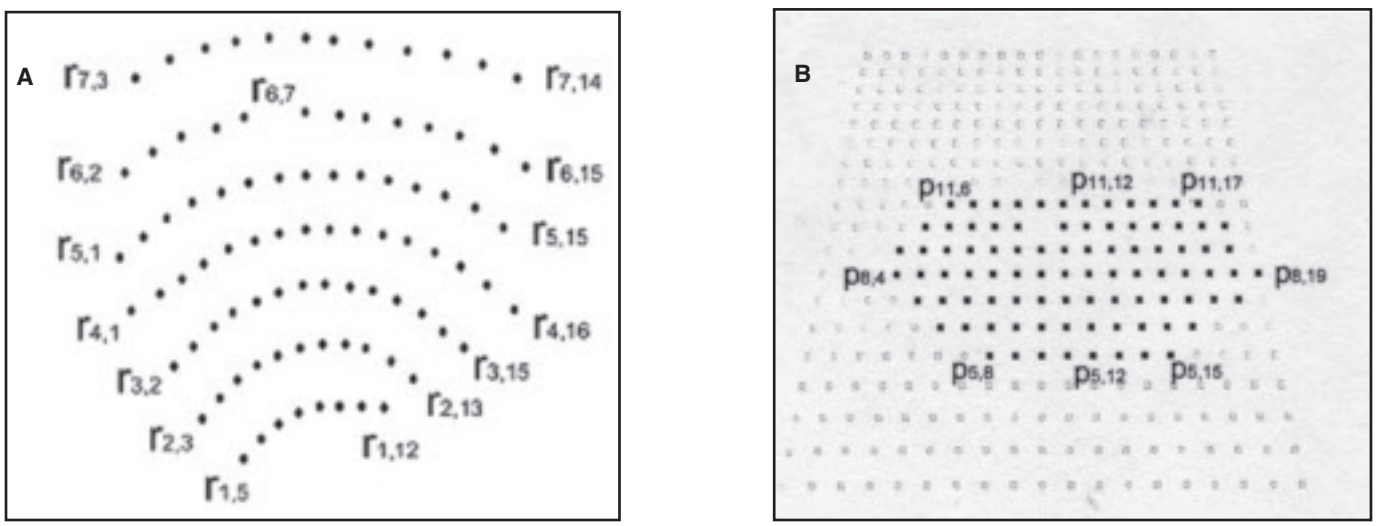

Fig. 4 — Reflected and projected dots S/S corresponding relationship. A — Row-column positions of reflected points; B — corresponding positions of projected dots in dot matrix.

ing algorithm and a feature extraction algorithm are proposed to process the reflected images (Ref. 14). First, the reflected points in the image are extracted in the point locating algorithm by using some image processing techniques, such as block thresholding segmentation (Ref. 15), median filtering, and morphological operations (Ref. 16). It can be seen in Fig. 3B, although the reflected pattern is distorted, the basic row-column relationship in the pattern remained.

Then based on the reflected dot positions, some image features, such as row-column relationship and the "center reference point" can be successfully determined by the feature extraction algorithm. For instance, there are 7 rows (curves) and 16 columns found in Fig. 3B and C. As shown in Fig. 3A, the center point of the 19×19 dot matrix (at the 10th row and the 10th column) is intentionally absent, and it is introduced as the center reference point to ease the matching process although it does not actually exist. In Fig. 3C, the corresponding position of the center reference point can be easily found in the 6th row.

To investigate the possible corresponding relationships between projected and reflected dots, a corresponding simulation was conducted (Ref. 14). In the simulation, part of a sphere was used to present the weld pool surface. By testing some convex and concave surfaces with typical dimensional values, it can be concluded that to produce the convex reflected images like Fig. 3B, the corresponding relationship for a convex surface is sequential/sequential (S/S) and the one for a concave surface is inverse/inverse (I/I). Here the relationship before the slash presents the column corresponding relationship, and the one after the slash presents the row corresponding relationship. In the proposed system, if the reflected column/row order is the same as that reflected from a flat surface, the relationship is defined as sequential; if the order is inversed, the relationship is inverse. Thus, combined with the corresponding position of reference point in the captured image, each reflected dot on the imaging plane can be successfully matched with a projected dot in the matrix by using the corresponding relationship. The matched point-ray pairs can be used to reconstruct the three-dimensional weld pool surface.

In Fig. 4, suppose $R=\{r_{k,t}, (k,t) \in I\}$ presents the set of reflected dots, on the reflected image I, and $P = \{p_{i,j}, (i,j) \in S\}$ presents the set of corresponding reflection dots on the weld pool surface S (here

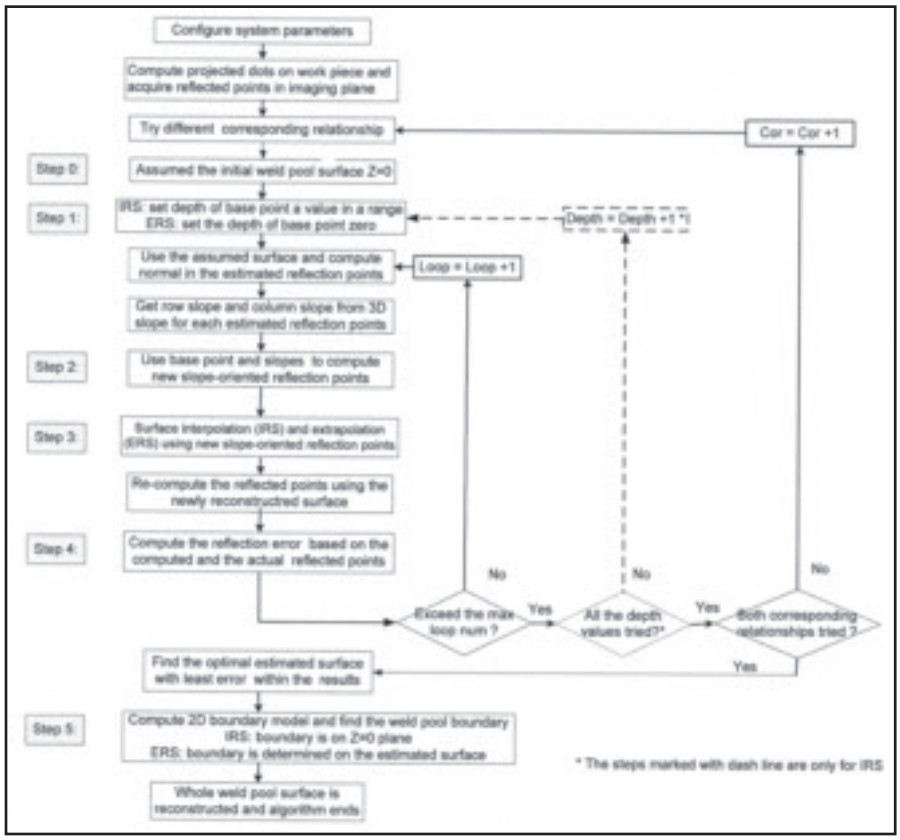

Fig. 5 — Flowchart of IRS and ERS.

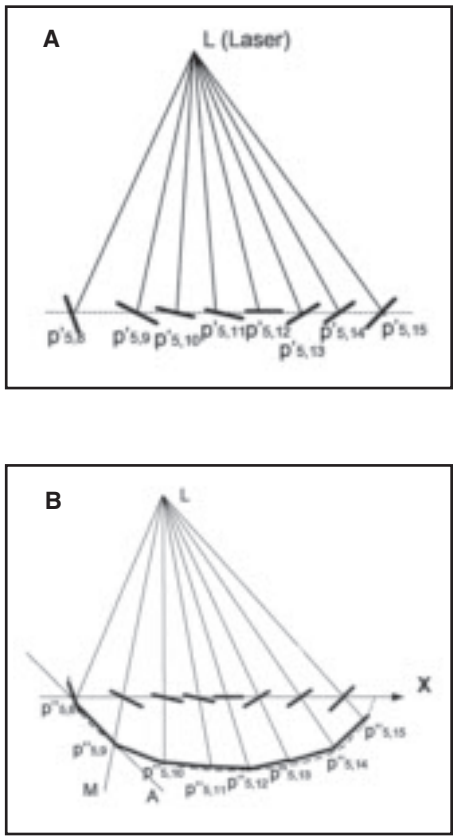

Fig. 6 — Computation of new slope-oriented reflection points based on base point in IRS. A — Row slopes of reflection dots on 5th row plane; B — computation of new reflection points using row slopes.

the subscripts present the row and column positions of the dots, and the numbers of dots in sets P and R are the same). The row-column position of the reflected dots are shown in Fig. 4A, and the corresponding position of the center reference point $p_{10,10}$ in the reflected image is $r_{6,7}$. If the corresponding relationship is I/I, the matched points pair is $r_{k,t} \leftarrow^{reflection} \rightarrow p_{10+6-k,10+7-t}$. If the corresponding relationship is S/S, the matched points pair is $r_{k,t} \leftarrow^{reflection} \rightarrow p_{k+10-6,t+10-7}$, and the corresponding reflection points are shown in Fig. 4B. For example, the corresponding projected point of reflected point $r_{1,5}$ is $p_{5,8}$. As can be seen, only those points that are actually projected on the liquid weld pool surface are reflected onto the imaging plane and are imaged and processed to reconstruct the weld pool surface in the proposed method, and those projected on the solid surface will not be reflected to and imaged on the imaging plane.

Reconstruction Schemes

From previous steps, two discrete sets of points ($R=\{r_{k,t},(k,t) \in I\}$, $P = \{p_{i,j},(i,j) \in S\}$) and their possible corresponding relationships were obtained. Now the task is to derive the three-dimensional weld pool surface from these matched discrete point sets based on the governing reflection law. It is apparent that the issue is not to apply the reflection law to calculate the reflection of incident rays. Instead, the issue here is to see what three-dimensional surface may generate a set of reflected points that are close enough to the given $R=\{r_{k,t},(k,t) \in I\}$. The issue is thus an inverse problem of the reflection law, and it appears an analytical solution does not exist.

To resolve this issue, an iterative engineering method is needed and the authors thus propose two schemes, interpolation and extrapolation reconstruction schemes (IRS and ERS), to find an optimally estimated three-dimensional surface. The ERS differs from the IRS in the way to construct the pool surface and determine the surface boundary. The details of the schemes proposed are presented below and the flowchart can be seen in Fig. 5.

Step 0: A flat plane (Z = 0) is used as the initial estimate of the weld pool surface. Since generally the depth of the weld pool is much smaller than its width and length for the GTAW process, it is reasonable to use a flat plane, i.e., Z = 0, as the initial estimate of the weld pool surface.

Step 1: Use the assumed surface to compute the slope field. Based on the results of corresponding simulation (Ref. 14), the tested corresponding relationships are chosen for the different shapes of reflected image. For example, for the "convex" image (Fig. 3B), two corresponding relationships (I/I and S/S) are tested sequentially, which can be seen in Fig. 5. Once the relationship is decided, the pairs of projected and reflected dots can be determined.

In the first step, the estimate of the weld pool surface was used to calculate the positions of the estimated reflection dots $p'_{i,j}$, in set P' ($P'=\{p'_{i,j}, (i,j) \in S\}$) where S is the assumed surface and i/j is the row/column number. Thus all the reflection lines are determined. By using the reflection law, the normal of every reflection point p'_{ij} on the surface can be further computed. Then the tangent plane of the surface at the reflection dot p'_{ij} can be obtained, which is referred to as its 3-D slope. This tangent plane intersects with the row plane and the column plane of dot $p'_{i,j}$ to find two tangent lines and the 3-D slope is thus decomposed into two 2-D slopes: row and column slopes. For example, in Fig. 6A the row slopes of reflection

dots at the 5th row are shown. Here the row/column plane of a dot refers to a plane passing through the laser diode and all the dots on the same row/column. These slopes of the estimated reflection dots form a slope field, which is used to produce the reflected image.

Step 2: Compute the new slope-oriented reflection points based on the slope field. It is obvious that the used surface in the first step cannot meet the slope requirements to produce the captured reflected image. Thus, in the second step the new slope-oriented reflection point set P'' ($P'' = \{p''_{ij}, (i,j) \in S\}$) is calculated to better approximate the actual weld pool surface based on these estimates of slopes.

Assumption of base point. In IRS and ERS, the positions of new slope-oriented reflection points are all calculated in relation to a base point, whose position is assumed. In IRS, the reflection point corresponding to the left-down reflected dot ($r_{1,5}$ in Fig. 4) is chosen as the base point. In Fig. 4, dot $p_{5,8}$ ($p'_{5,8}$ or $p''_{5,8}$) is the base point for S/S corresponding relationship. In IRS, the height of the base point is sequentially selected in a range, such as (–0.5 mm, 0.5 mm). While in ERS, the base point is chosen according to different corresponding relationships so as to make it on the left head part of the weld pool surface. For instance, in Fig. 4B $p_{11,6}$ ($p'_{11,6}$ or $p''_{11,6}$) is the base point for S/S corresponding relationship in ERS. The height of the base point can be reasonably assumed to be zero instead of searching in a range since the base point is on the boundary of the head of the weld pool surface.

Computation of new slope-oriented reflection points. Based on the selected base point, all the other reflection points on the pool surface can be calculated. There are three computation procedures for ERS and IRS as shown in Fig. 7. First, the new slope-oriented reflection dots on the same row as the base point are computed using their row slopes. In Fig. 6, the new reflection points at the 5th row are computed by using their row slopes in IRS. Since the position of base point $p''_{5,8}$ is decided, the adjacent dot $p''_{5,9}$ can be located as the intersection point of projected ray LM and line $p''_{5,8}A$, and the slope of line $p''_{5,8}A$ can be decided as Equation 1

$$S_{p''_{5,8}A} = sign\left(S_{p''_{5,8}}\right) \cdot \left| \left(S_{p''_{5,8}A} + S_{p''_{5,9}}\right)/2 \right| \quad (1)$$

where the function sign () means the positive or negative sign of the slope and $S_{p''5,8}$ and $S_{p''5,9}$ refer to the row slopes of the reflection point of $p''_{5,8}$ and $p''_{5,9}$, respectively. Following the same procedures, all the other reflection points in the 5th row can be calculated as shown in Fig. 6B. Then based on the middle point of the row with base point ($p''_{5,12}$ and $p''_{11,12}$ for IRS and ERS), the middle points at the same column (12th column), but different rows can be calculated by using column slopes just as done in the previous step. At last, row slopes are used to compute the positions of all the other new reflection points based on the positions of the middle points at their rows. Thus, the positions of all updated reflection dots are calculated by using the computed slope field.

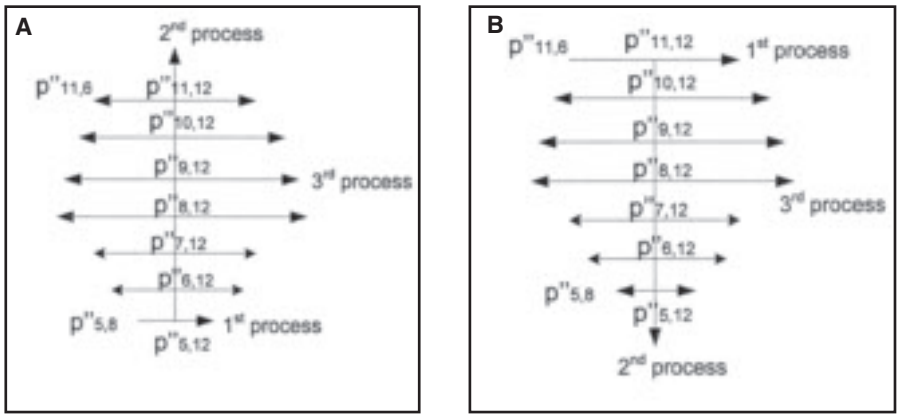

Fig. 7 — Steps of computing new reflection points. A — For IRS; B — for ERS.

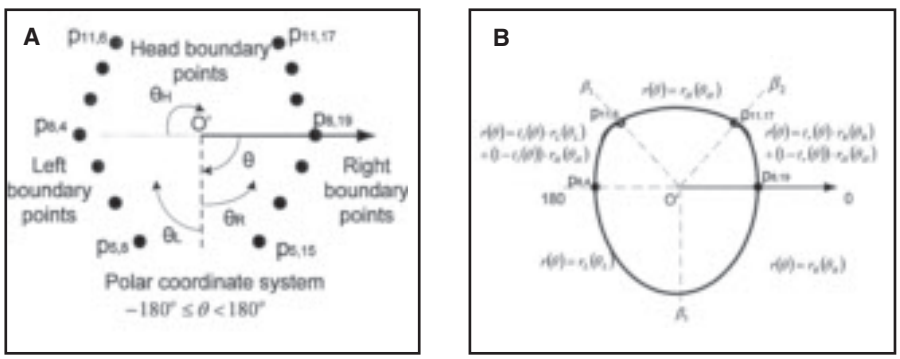

Fig. 8 — 2-D boundary piecewise model. A — Boundary points; B — five parts of the boundary model.

Step 3: Reconstruction of weld pool surface using new reflection points. In the third step, a weld pool surface should be deduced depending on the reflection points P'' computed in the second step. Here the interpolation method (Ref. 17) is used in IRS and the method (Ref. 18) that can realize both interpolation and extrapolation is applied in ERS. They both can produce a smooth surface from nonuniformly sampled data in the form of Equation 2.

$$z = f(x,y) \quad (2)$$

In IRS the area of reconstructed surface is limited by the reflection points while in ERS the area of the reconstructed surface is not, which makes their ways to determine boundary different.

Step 4: Compute the error of the reconstructed surface. In the fourth step, based on the knowledge of the projected dot matrix and the surface reconstructed in the third step, the reflected points set R' ($R' = \{r'_{k,t}(k,t) \in I\}$) on the imaging plane can be recomputed and compared with the positions of the captured reflected point set R. The distances between the actual and computed reflected points can thus be calculated and be further mapped to the weld pool surface as "reflection error," which is discussed later. After error calculation, the estimated surface in Step 3 is used as the new assumed surface to continue the first step within pre-set loops for each corresponding relationship. At last, after all possible corresponding relationships are tried, the computed surface with the minimum reflection error is chosen as the optimally estimated weld pool surface.

Step 5: Calculate 2-D surface model and use it to find the weld pool boundary. In this step, a two-dimensional piece-wise boundary model $r(\theta)$ in a polar coordinate system is developed to determine the three-dimensional boundary of the weld pool surface. First, the two end points in each reflection row are selected as bound-

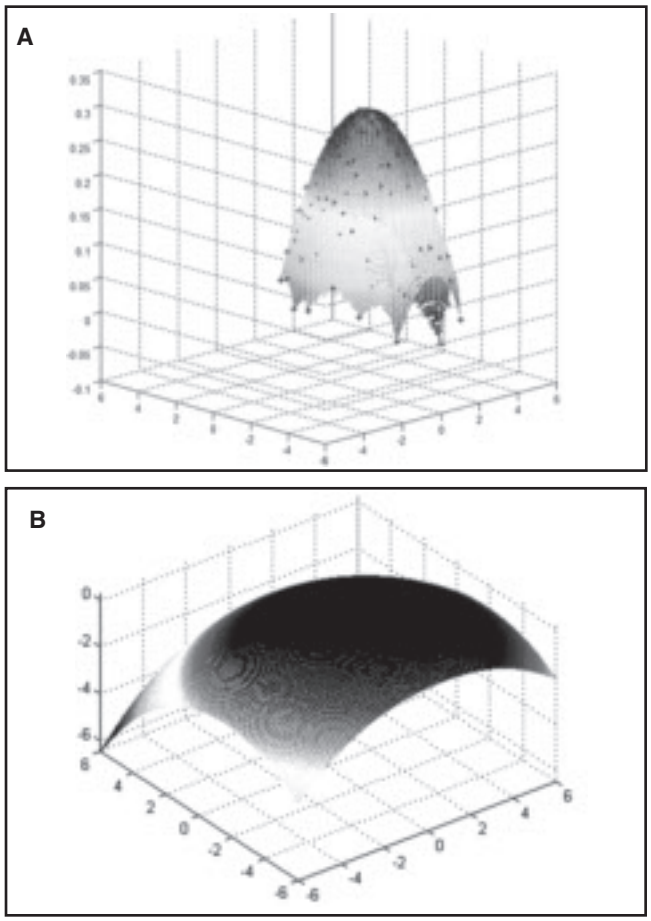

Fig. 9 — Optimal estimated weld pool surface. A — The interpolation result of IRS; B — the extrapolation result of ERS.

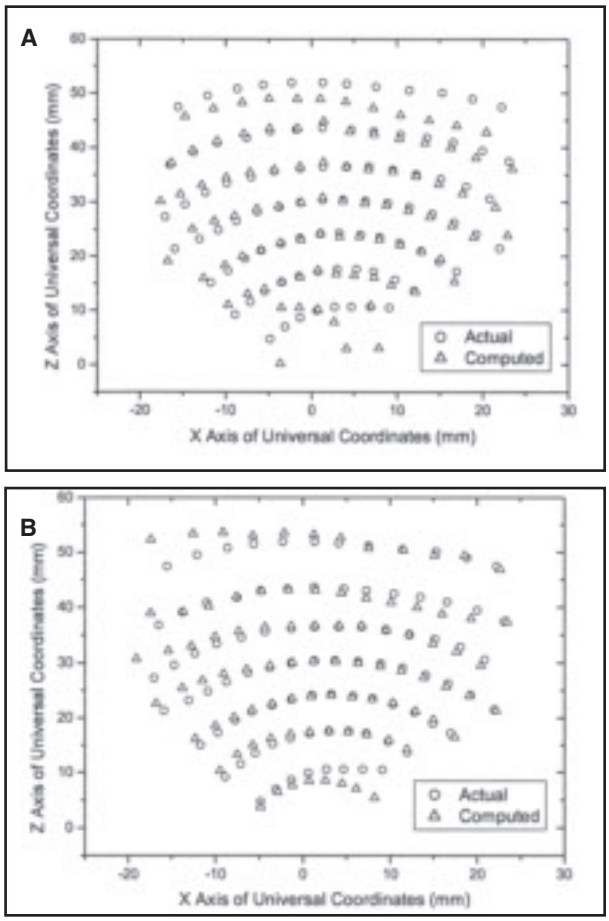

Fig. 10 — Computed and actual reflected points compare using different schemes. A — Result of IRS; B — result of ERS.

ary points in Fig. 4B, and they are classified into three sets: left (L), right (R), and head (H) sets as shown in Fig. 8A. Here, S/S corresponding relationship is assumed, and the origin of the system is chosen as the middle point of the longest row (8th row in Fig. 8). Then the polar coordinate models in Equation 3 are used to describe the three parts (left, right, and head part) of the weld pool boundary. The points in three sets can be used to fit the models respectively and the coefficients ω_i can thus be decided by using the mean square method.

$$r_H(\theta_H)=\omega_{H0}+\sum_{i=1}^{3}\left(\omega_{H\,i}\cdot\theta_H^i\right)$$
$$r_L(\theta_L)=\omega_{L0}+\sum_{i=1}^{3}\left(\omega_{L\,i}\cdot\theta_L^i\right)$$
$$r_R(\theta_R)=\omega_{R0}+\sum_{i=1}^{3}\left(\omega_{R\,i}\cdot\theta_R^i\right) \quad (3)$$

At last, the whole two-dimensional piecewise boundary model of the weld pool surface can be expressed by Equation 4. As shown in Fig. 8B, it is composed of five segments (including two transition segments).

$$r(\theta)=r_H(\theta_H)=r_H(\theta+180\ \text{deg}) \quad \beta_1\le\theta\le\beta_2$$

$$r(\theta)=t_L(\theta)\cdot r_L(\theta_L)+(1-t_l(\theta))\cdot r_H(\theta_H)=t_l(\theta)\cdot r_L(0+270\ \text{deg})+(1-t_l(\theta))\cdot r_H(\theta+180\ \text{deg}) \quad -180<\theta<\beta_1$$

$$r(\theta)=r_L(\theta_L)=r_L(\theta-90\ \text{deg}) \quad \beta_3\le\theta\le 180$$

$$r(\theta)=t_R(\theta)\cdot r_R(\theta_R)+(1-t_r(\theta))\cdot r_H(\theta_H)=t_r(\theta)\cdot r_R(90\ \text{deg}-\theta)+(1-t_r(\theta))\cdot r_H(\theta+180\ \text{deg}) \quad \beta_2<\theta<0$$

$$r(\theta)=r_R(\theta_R)=r_R(90\ \text{deg}-\theta) \quad 0\le\theta<\beta_3 \quad (4)$$

where $t_l(\theta)$ and $t_r(\theta)$ are the weights that are defined as Equation 5

$$t_l(\theta)=(\beta_1-\theta)/(\beta_1+180\ \text{deg}) \quad -180\le\theta\le\beta_1$$
$$t_r(\theta)=1-\theta/\beta_2 \quad \beta_2\le\theta\le 0 \quad (5)$$

where β_1, β_2,0 deg, 180 deg, and β_3 are the boundaries for the segments. β_1 is defined as the largest angle of the boundary point among (–180 deg, –90 deg) in set L. β_2 is defined as the smallest angle of the point in set R, and β_3 is the intersection angle of left segment $r_L(\theta_L)$ and right segment $r_R(\theta_R)$. In IRS, the computed 2-D boundary model in Z = 0 plane is assumed to be the weld pool surface boundary. For ERS since the reconstructed weld pool surface is extrapolated, it is possible to find a more reasonable boundary based on the proposed model. In ERS the established 2-D boundary model is used to determine the X and Y coordinates of the boundary on the optimally estimated surface. At last, the newly found boundary points together with the optimal reflection points are used by the interpolation method to get the new whole weld pool surface.

Reconstruction Results

In this section, a reflected image shown in Fig. 3B is used to test IRS and ERS. The results of the two schemes are compared and discussed. As can be seen, an iteration process is used in IRS and ERS to find the optimally estimated surface according to the computed error. To define a meaning-

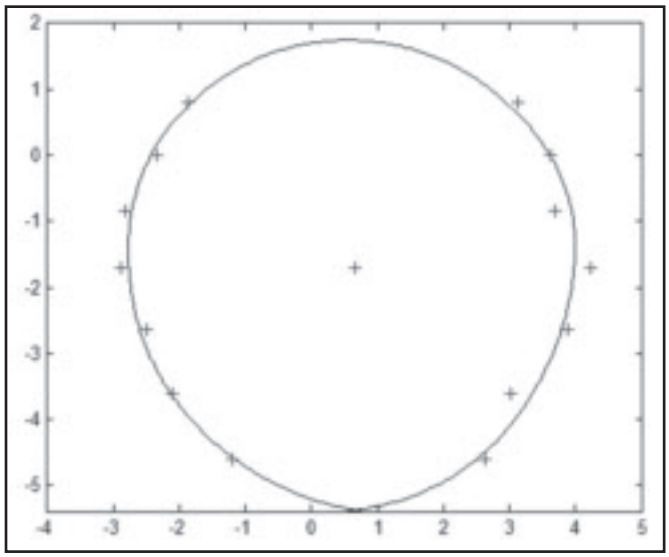

Fig. 11 — Fitted two-dimensional weld pool boundary model (on Z = 0 plane).

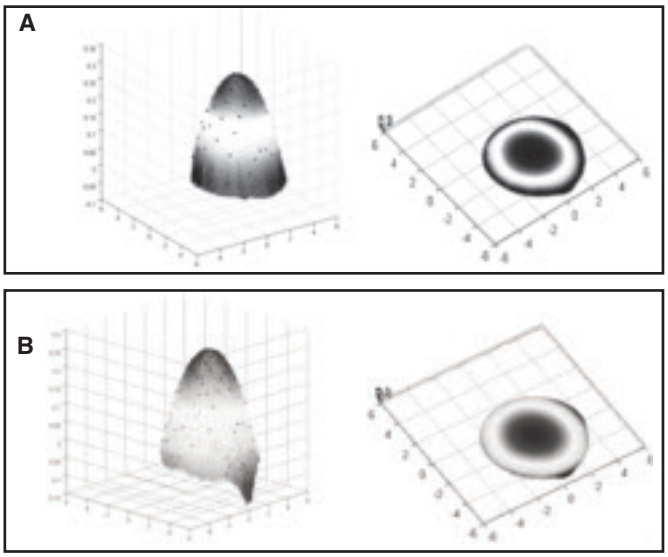

Fig. 12 — Results of different reconstruction schemes. A — Weld pool surface using interpolation reconstruction scheme (different views); B — weld pool surface using extrapolation reconstruction scheme (different views).

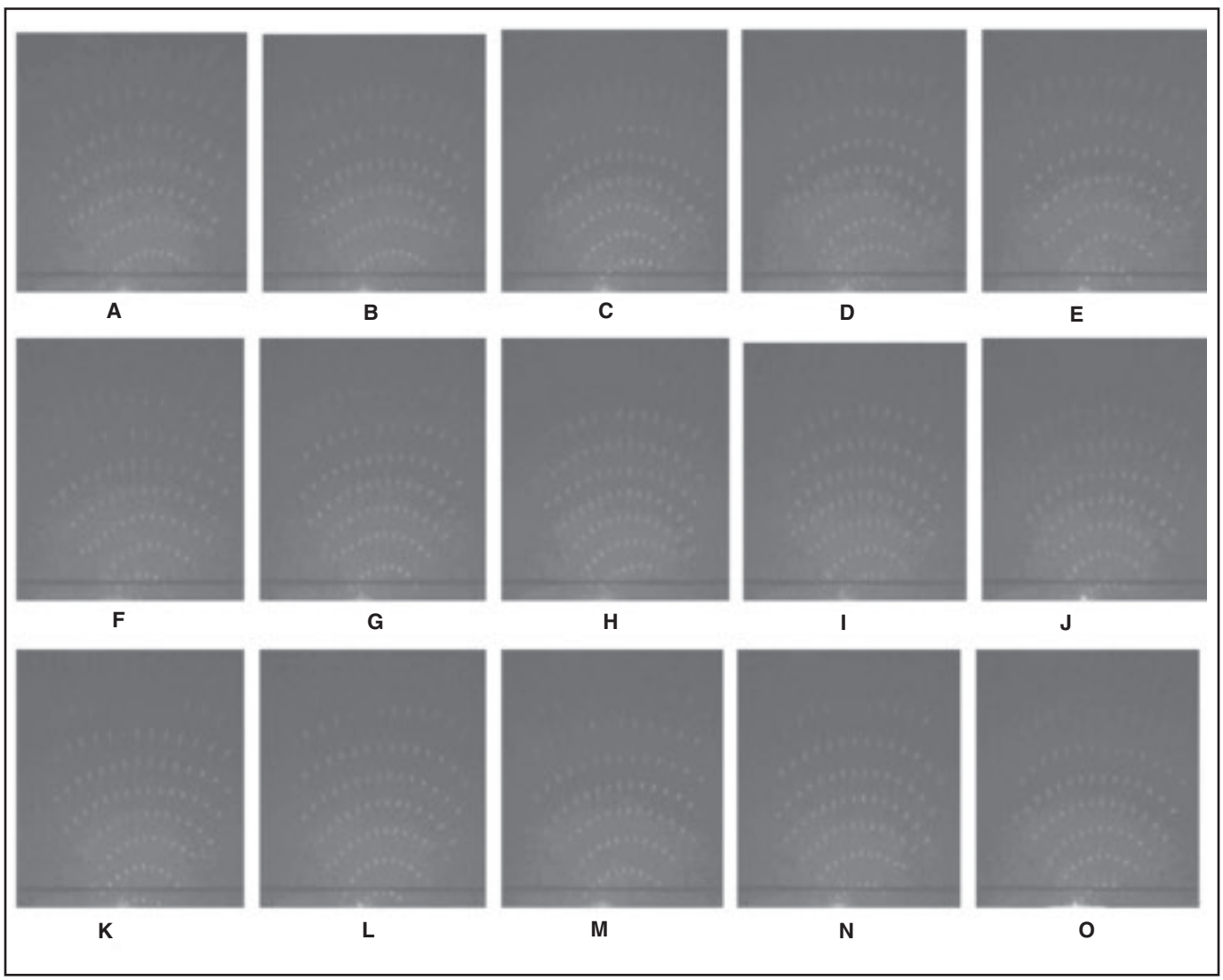

Fig. 13 — Captured reflected images.

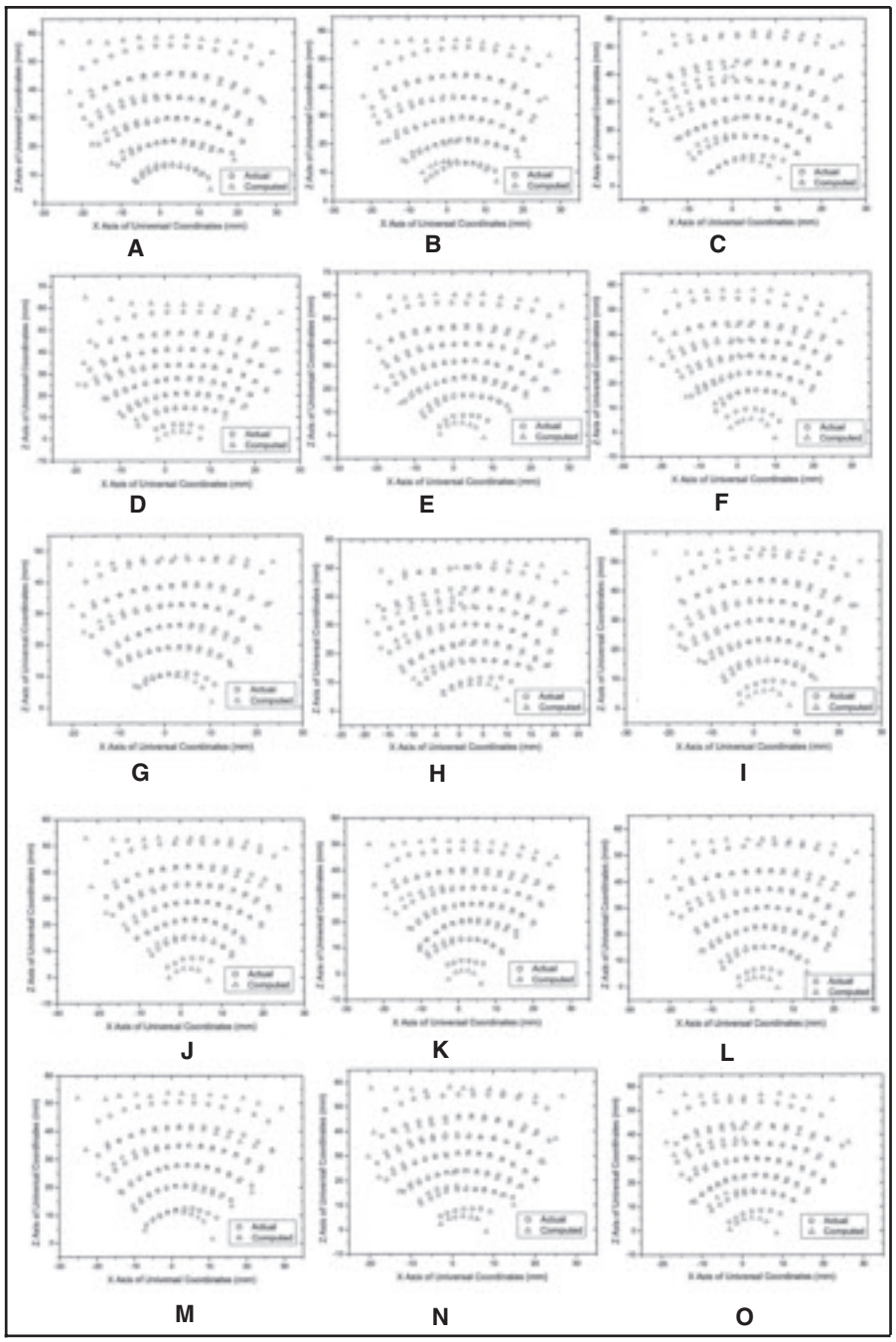

Fig. 14 — Computed and actual reflected points comparison.

ful error that can describe the difference between the calculated and actual reflection points on weld pool surface, the authors propose an error measurement parameter: average reflection error (ARE). Its definition is shown in Equation 6.

$$ARE = \sum_{k,t} E_{k,t} / n, \ldots \left(k,t\right) \in I \quad (6)$$

where I refers to the reflected image and n represents the total number of the reflected points on the imaging plane. $E_{k,t}$ represents the reflection error for the corresponding reflection point of $r_{k,t}$, and it is defined as Equation 7.

$$E_{k,t} = \sqrt{\left(e^x_{k,t} \bullet \frac{W_p}{W_r}\right)^2 + \left(e^z_{k,t} \bullet \frac{L_p}{L_r}\right)^2} \quad (7)$$

where $e^x_{k,t}$ and $e^z_{k,t}$ are the distances between estimated reflected point $r'_{k,t}$ and actual reflected point $r_{k,t}$ along horizontal direction (X axis) and vertical direction (Z axis) on the imaging plane. W_r and L_r represent the horizontal and vertical ranges of the reflected dots, and W_p and L_p represent the horizontal (X axis) and vertical (Y axis) ranges of the corresponding projected dots on the workpiece (Z = 0). It can be seen the error parameter ARE effectively maps the difference between calculated and actual reflected points to the error of the reflection points on the weld pool surface.

The optimal surfaces by using IRS and ERS are shown in Fig. 9, and their corresponding relationships are all S/S. By using extrapolation reconstruction scheme (ERS), the computed minimal average reflection error (ARE) is 0.1234 mm, which is a little smaller than the result of IRS 0.1691 mm. In IRS, the smallest ARE is achieved when the height of the base point is 0. It can be seen that the area of optimally interpolated surface reconstructed by IRS is limited by the reflection points, but it is not the case for ERS.

In Fig. 10, the positions of actual reflection points and computed reflected points using optimally estimated surface are shown for the two schemes. These two results are similar, but for the matching extent of edge points, the performance of ERS is better since the extrapolation method works better than interpolation to deduce the boundary. One thing should be noted here. The absent dot $r_{6,7}$, which corresponds to the center reference point in Fig. 4, is still considered as a reflected point in the schemes, and its position is assumed in the middle of its adjacent two dots in the 6th row in Fig. 10.

Based on the results of interpolation or extrapolation reconstruction methods and the Sequential/Sequential (S/S) corresponding relationship, the fitted two-dimensional (2-D) boundary (at Z = 0 plane) shown in Fig. 11 is used to find the boundary points. The point in the center is the origin of the used polar coordinate system for the model, and it is defined as the center point of the weld pool. The shape of the modeled 2-D boundary is similar as the ones shown in Fig. 1. Because the welding speed is slow (3 mm per second), the difference between width (6.7313 mm) and length (7.1182 mm) is small and the 2-D shape is like a circle, which can be verified by the measurement result after the experiment. Since the welding electrode is on the Z axis, it can be found in Fig. 11 that the distance between the coordinate origin and the weld pool head is smaller than the distance to its tail.

In Fig. 12, the whole 3-D weld pool surfaces are reconstructed by using both the boundary model and the optimally estimated surfaces in IRS and ERS. The two reconstructed surfaces are both convex. (This is probably related to the properties of the mild steel workpiece.) The heights of the surfaces are 0.3045 mm and 0.2533

mm, respectively, in Fig. 12A and B. The difference is small, while the difference between their boundaries is obvious due to different ways to compute the boundary. The result of the extrapolation reconstruction scheme is more reasonable since the boundary is not exactly on Z = 0 plane.

Analysis of Variations in Weld Pool Surface

A series of reflected images are recorded during an experiment using the same nominal constant welding parameters in order to examine if the weld pool surface would remain unchanged. Figure 13 shows reflected images at a rate of 60 frames per second. During this experiment, a sheet of 2-mm-thick mild steel was used as the workpiece and the welding current was 75 A with a constant welding speed of 3 mm/s. The distance between the torch and imaging plane was 50 mm, and the projection angle of laser diode was about 31 deg. From the reflected images, the shape changes of the weld pool surface can be seen clearly. The first variation is the number of rows of reflected dots, which varies from 6 to 8. This means the length of the weld pool surface is changing. The second change is the corresponding position of the center reference point in the reflected images, which shows the position change of the weld pool surface. Even when the number of rows is the same in some images, the number of dots in a row still changes. It reflects the variation of width in the weld pool surface. These deductions are drawn based on the facts that projected laser dot matrix covers the whole weld pool surface immovably and only the dots on the pool surface can be reflected onto the imaging plane.

In order to further investigate the variation of weld pool quantitatively, the extrapolation reconstruction scheme (ERS) was applied to reconstruct the weld pool surface for each reflected image in Fig. 13. One thing should be noted here. In our study, some unclear dots located in upper fragmental rows are neglected since some dots in the row are blocked by the torch and they are not suitable for the proposed reconstruction schemes, such as the ones in Fig. 13H, K, and M. By using the ERS, the optimal estimates of three-dimensional weld pool surfaces are reconstructed for each reflected image in Fig. 13, and the differences between computed reflected images by using optimally estimated surfaces and the actual captured ones are shown in Fig. 14.

After the computation of the two-dimensional boundary model, the whole weld pool surface can be reconstructed by using ERS. The results are shown in Fig. 15. The shapes variation of these reconstructed surfaces can be clearly seen. In Fig. 16, the computed average reflection errors (ARE) for different reflected images vary insignificantly in a range of (0.13632 mm, 0.23247 mm).

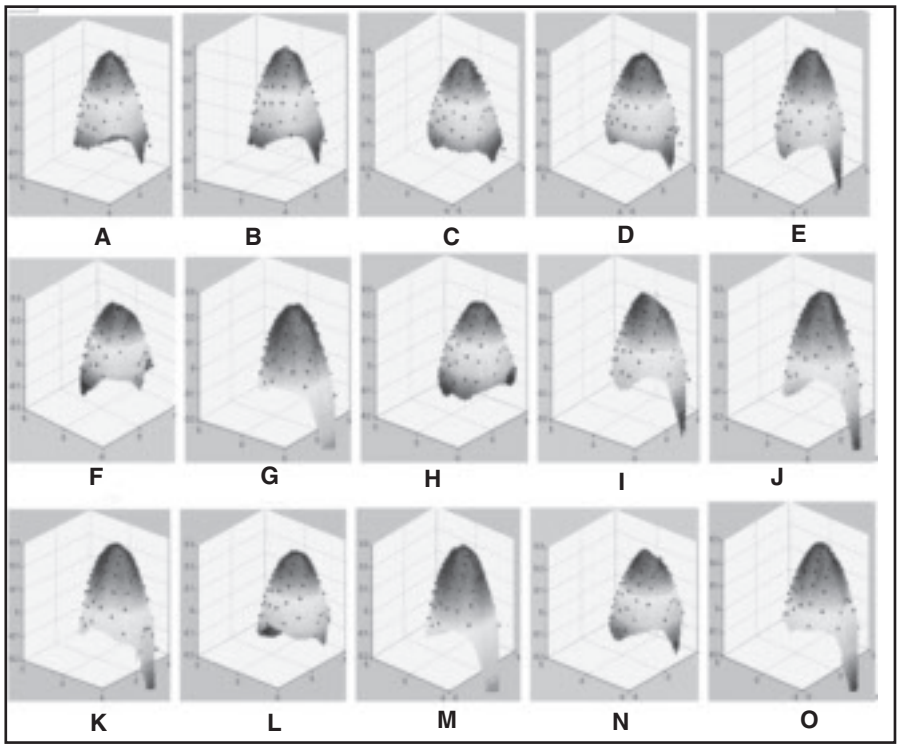

Fig. 15 — Reconstructed three-dimensional weld pool surfaces.

Figure 17 shows the variations of two-dimensional parameters of the reconstructed weld pool: the width and the length, which are decided by the boundary model. The width of the weld pool surface varies in the range of 6.4463 to 6.9183 mm, or ±3.5%. The average width and its variance are calculated as Equation 8.

$$\bar{w} = E\left(w\right) = \sum_{i=1}^{15} w_i / 15 = 6.6645\,mm,$$

$$V_w = E\left(\left(w_i - \bar{w}\right)^2\right) = \sum_{i=1}^{15}\left(w_i - \bar{w}\right)^2 / 15 = \left(0.15\right)^2\,mm^2 \quad (8)$$

where w_i represents the width of the i^{th} reconstructed weld pool surface. The length of the pool surface varies in the range of 7.1303 to 8.1092 mm or ±6.4%. The average length and its variance are shown in Equation 9.

$$\bar{l} = E\left(l\right) = \sum_{i=1}^{15} l_i / 15 = 7.4549\,mm,$$

$$V_l = E\left(\left(l_i - \bar{l}\right)^2\right) = \sum_{i=1}^{15}\left(l_i - \bar{l}\right)^2 / 15 = \left(0.46\right)^2\,mm^2 \quad (9)$$

where l_i presents the length of the i^{th} reconstructed weld pool surface. It can be seen that the variation of weld pool surface length is greater than that of the width.

Figure 18 shows the height variation of the weld pool surface. Since the reconstructed surfaces are all convex, and the Z coordinate of the highest point in the surface is considered as the height of the weld pool surface. From the figure, it can be seen the heights of the surfaces vary from 0.2514 to 0.3238 mm or in the range of ±12.6%. The average height and variance are shown in Equation 10.

$$\bar{h} = E\left(h\right) = \sum_{i=1}^{15} h_i / 15 = 0.2943\,mm,$$

$$V_h = E\left(\left(h_i - \bar{h}\right)^2\right) = \sum_{i=1}^{15}\left(h_i - \bar{h}\right)^2 / 15 = \left(0.019\right)^2\,mm^2 \quad (10)$$

where h_i represents the height of the i^{th} reconstructed surface. The relative variation of the height is thus much greater than those of the width and length.

In Fig. 19, the variation of the weld pool positions is shown. It also can be seen that the positions of the center point and the highest point of the weld pool surface are also changing for the studied images. The position of the center point of the weld pool is shown in Fig. 11. The variations of these three-dimensional parameters discussed above prove that the weld

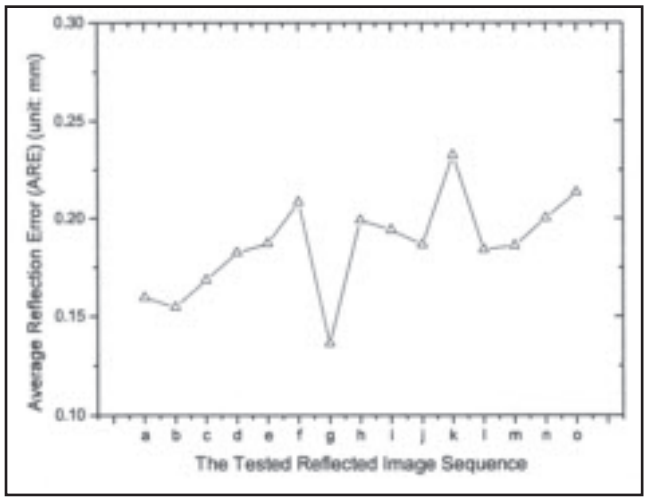

Fig. 16 — Average reflection errors (ARE).

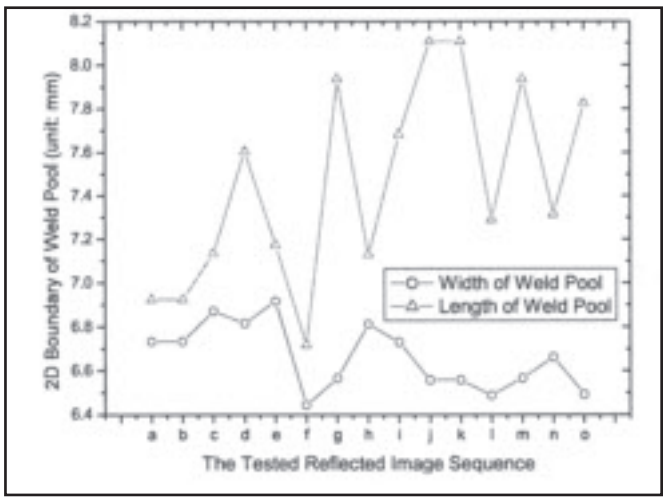

Fig. 17 — Variation of weld pool width and length.

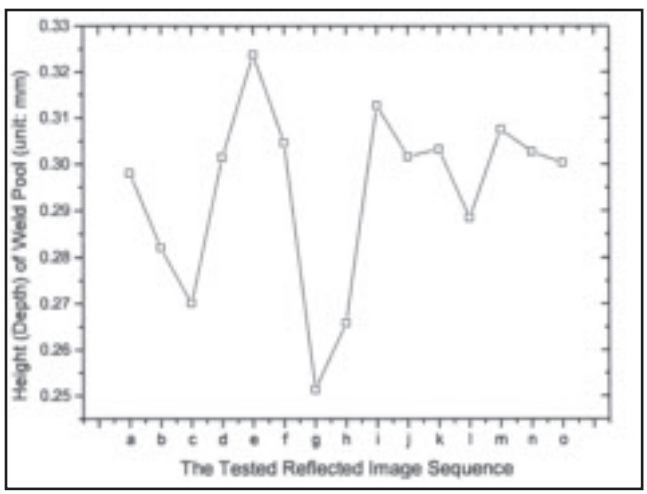

Fig. 18 — Variation of the pool surface height (depth).

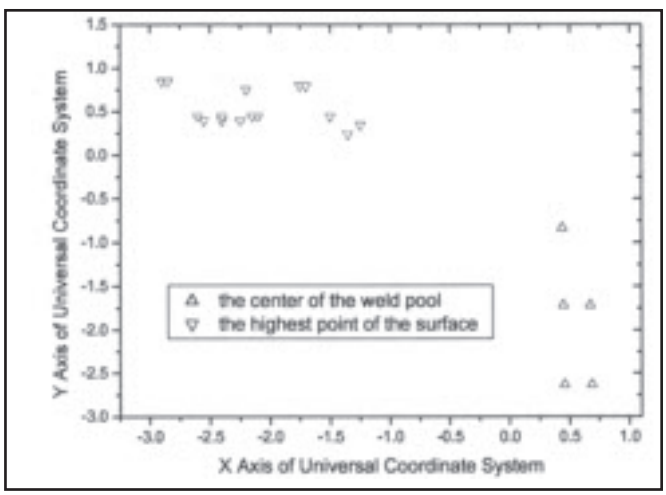

Fig. 19 — Variation of the weld pool positions.

pool surface has fluctuations even in the same nominal welding conditions. The possible reasons include the possible small fluctuations in the welding current and speed, possible shielding gas turbulence, and other possible interference factors.

Discussion

Although the reconstruction results of the three-dimensional weld pool surface proved the effectiveness of the proposed system, the accuracy of the reconstructed surface still needs to be discussed. In section 4, the reconstructed pool surfaces are shown in Fig. 12. There is no obvious concave region inside the weld pool surface under the torch, which is practical because of the arc pressure. The possible explanation is that the concave region in the weld pool surface is very small due to the low welding current (75 A) and/or there is no laser dots projected onto it.

In previous discussion, it was seen that some slightly concave regions exist among upper rows in some of the reflected images in Fig. 13, and the irregular concave regions are embedded in some of the reconstructed weld pool surfaces in Fig. 15. Figure 20 shows some of those cases corresponding to Fig. 13B, E, and N. For example, in Fig. 20A the reflected dots at 4th, 5th, and 6th row form nonsmooth convex curves with slightly concave regions, which gives the reconstructed surface an obvious concave region inside it. The possible reason is the variation of the weld pool surface makes more rays project onto the small concave region of the surface. Although the errors of optimal results are small, obvious differences between the reflected images still can be seen in Figs. 10 and 14. Since it is a sensing system for a small object, there are many factors in the scheme that may cause errors, such as the parameter measurement, image processing, the surface interpolation/extrapolation, and boundary modeling process. Thus, an error analysis of the proposed system is needed, and future work should be done to improve the accuracy of the reconstructed three-dimensional weld pool surface.

Conclusions

A sensing system has been proposed to image the reflection of projected laser pattern from the specular weld pool surface. To derive the three-dimensional weld pool surface based on the image processing results, two reconstruction schemes (IRS and ERS) are proposed for off-line computation. Based on the studies and analyses in this paper, the following conclusions can be drawn:

- The proposed reconstruction schemes can be used to resolve the inverse problem of the reflection law to derive the three-dimensional weld pool surface from the image processing results.
- The proposed error measurement

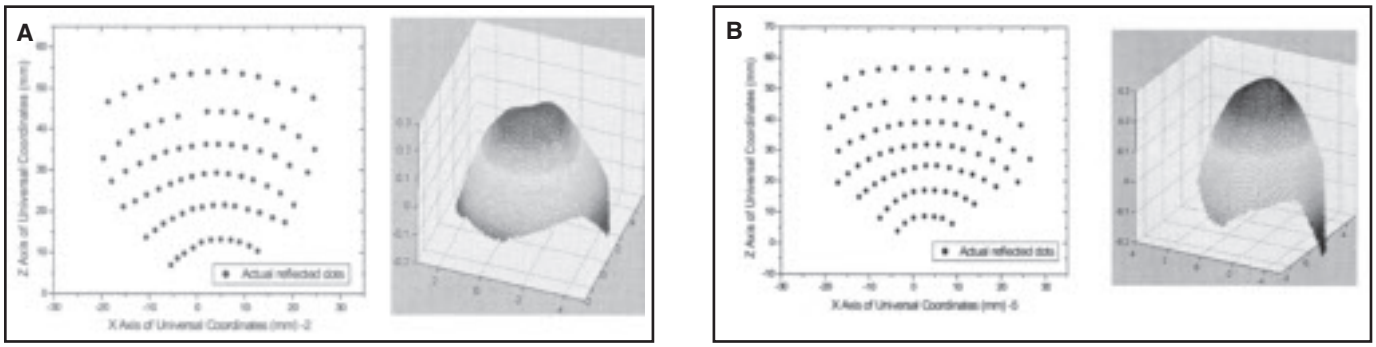

Fig. 20 — Examples of reconstructed weld pool surfaces embedded with concave parts. A — Reflected image and reconstructed surface of Fig. 13B; B — reflected image and reconstructed surface of Fig. 13E; C — reflected image and reconstructed surface of Fig. 13N.

parameter provides an effective way to estimate and quantify the accuracy of the resultant weld pool surface and the convergence of the solution.

• In ERS, the base point is chosen on the head of weld pool surface, and its height is reasonably assumed zero. The iterative search process used in IRS can thus be avoided and the reconstruction speed is improved accordingly.

• In comparison with interpolation reconstruction scheme (IRS), the extrapolation reconstruction scheme (ERS) can achieve better accuracy especially for the rear of the weld pool surface.

• Through applying ERS to a series of reflected images acquired from an experiment with nominal constant welding parameters, the variations of the three-dimensional weld pool surface are studied. It is found that the variation of the length is greater than that of the weld pool width, and the relative variation of the height (depth) of the weld pool surface is much greater in comparison with those of the length and width.

Acknowledgments

This research was funded by the National Science Foundation under Grant DMI-0527889 Sensors: Measurement of Dynamic Weld Pool Surface. HongSheng Song also thanks the University of Kentucky Graduate School for the financial support through the Kentucky Opportunity Scholarship.

References

1. Groenwald, R. A., Mathieson, T. A., Kedzior, C. T., and Gaid, I. N. C. 1979. Acoustic emission weld monitor system — data acquisition and investigation. U.S. Army Tank-Automotive Research and Development Command Report ADA085-518.

2. Siores, E. 1988. Development of a real-time ultrasonic sensing system for automated and robotic welding. PhD thesis, Brunel University.

3. Guu, A. C., and Rokhlin, S. 1989. Computerized radiographic weld penetration control with feedback on weld pool depression. *Mater. Eval.* 47: 1204–10.

4. Saeed, G. M. 2005. *Three-dimensional Measurement of Specular Surfaces and Its Application in Welding Process*. PhD thesis, University of Kentucky.

5. Richardson, R. W., et al. 1984. Coaxial arc weld pool viewing for process monitoring and control. *Welding Journal* 63(3): 43–50.

6. Agapakis, J. E., and Bolstad, J. 1991. Vision sensing and processing system for monitoring and control of welding and other high luminosity processes. *International Robots & Vision Automation Conf.*, pp. 23–29.

7. Kovacevic, R., Zhang, Y. M., and Ruan, S. 1995. Sensing and control of weld pool geometry for automated GTA welding. *ASME Journal of Engineering for Industry* 117(2): 210–222.

8. Kovacevic, R., and Zhang, Y. M. 1997. Real-time image processing for monitoring of free weld pool surface. *ASME Journal of Manufacturing Science and Engineering* 119(2): 161–169.

9. Mnich, C., Al-Bayat, F., Debrunner, C., Steele, J., and Vincent, T. 2004. In situ weld pool measurement using stereovision. *ASME, Proceedings 2004, Japan–USA Symposium on Flexible Automation*, Denver, Colorado.

10. Yoo, C. D., and Lee, J. 3D measurement of weld pool using biprism stereo vision sensor, *http://joining1.kaist.ac.kr/research/vision.htm,* Seoul National University.

11. Zhao, D. B., Yi, J. Q., Chen, S. B., Wu, L., and Chen, Q. 2003. Extraction of three-dimensional parameters for weld pool surface in pulsed GTAW with wire filler. *ASME J. Manuf. Sci. Eng*. Vol. 125, pp. 493-503.

12. Zhang, Y. M., Song, H. S., and Saeed, G. 2006. Observation of a dynamic specular weld pool surface. *Measurement Science & Technology* 17(6): L9–L12.

13. Song, H. S., Saeed, G., and Zhang, Y. M. 2006. Observation of dynamic specular weld pool surface. *Proceedings of 2006 ISFA (International Symposium on Flexible Automation)*, 0252-b(S) pp. 661–662, Osaka, Japan.

14. Song, H. S., and Zhang, Y. An image processing scheme for measurement of specular weld pool surface. *Welding Journal* 86(10): 241-s to 249-s.

15. Snyder, W. E., and Qi, H. 2004. *Machine Vision*, Cambridge University Press, ISBN 052183046X.

16. Gonzalez, R. C., and Woods, R. E. 2002. *Digital Image Processing*, second edition, Prentice Hall.

17. Barber, C. B., Dobkin, D. P., and Huhdanpaa, H. T. 1996. The quickhull algorithm for convex hulls. *ACM Transactions on Mathematical Software* 22(4): 469–483.

18. Sandwell, D. T. 1987. Biharmonic spline interpolation of GEOS-3 and SEASAT altimeter data. Geophysical Research Letters 2: 139–142.